Chapter 5

PLL-Less Control Strategy of a Grid-Tied PV System Under Distorted Grid, Weak Grid and Grid Fault Conditions

5.1 Introduction

In the previous chapter, an advanced PLL-less control strategy is proposed to reduce grid current harmonics and eliminate power oscillations of a grid-tied PV system under distorted grid voltage conditions. However, its performance deteriorates in grid fault conditions that require low voltage ride through (LVRT) capability. Further, in weak grid conditions that offer a large value of grid impedance, previous chapters' control strategy does not satisfactorily suppress the current harmonics. Moreover, the grid-tied PV system with a conventional proportional multi-resonant (CPMR) controller cannot maintain stability under a weak grid due to the negative influence of PLL. To take care of these issues of grid-tied PV systems, this chapter presents a PLL-less phase shifted proportional multi-resonant controller for a grid-tied PV system. The proposed PLL-less control strategy enhances the LVRT capability along with reduced grid current harmonics and power oscillations. The proposed control strategy achieves enhanced LVRT operation of the grid-tied PV system by incorporating an active power regulator (APR) with dynamic reactive power support (DRPS) controller. An advanced phase compensated multi-resonant (APCMR) controller is integrated with the APR with DRPS controller to suppress the grid current harmonics under weak and distorted grid voltages in this chapter. Further, to eliminate active and reactive power oscillations at the grid side caused by the grid faults, a phase-compensated reference current generator (PCRCG) is integrated with the proposed control strategy. As the synchronization mechanism of the grid-tied PV system is included in PCRCG, the requirement of PLL can be avoided in this method. Thus, the associated computational burden on the digital microcontroller is reduced. The effectiveness of the proposed control strategy is validated using the OPAL-RT digital simulator and offers superior performance compared to the conventional PLL-based control strategy.

5.2 System Architecture of PLL-Less Grid-Tied PV System

The system architecture of the proposed PLL-less control strategy with APCMR current controller for a single-stage grid-tied PV system is shown in Fig. 5.1. At the point of interconnection, the PV array is linked to the grid through a VSI and an LCL filter. The grid-tied PV system is comprised of a single-stage that uses the VSI to harvest the

maximum power from the PV array and deliver it to the grid. The different schemes of the overall control structure of the grid-tied PV system is categorized into four different modules, namely i) DC-link voltage controller, ii) active power regulator (APR) with dynamic reactive power support (DRPS) controller, iii) advanced phase compensated multi-resonant (APCMR) current controller and (iv) phase compensated reference current generator (PCRCG). The DC-link voltage controller regulates the DC-link voltage by adjusting the active power P_g injected into the grid. The APR with DRPS controller regulates the injection of P_g and reactive power Q_g during grid fault. To limit the P_g injection from the PV array, the PV voltage is regulated using flexible power point tracking (FPPT) controller by keeping the magnitude greater than the maximum power point voltage V_{MPP}. The APCMR controller has a phase leading angle in the resonant controller to improve the system stability, reduce the steady-state error in grid current and suppress the grid current harmonics under distorted and weak grid conditions. The PCRCG is used to provide the reference value of grid current $i_{g\alpha\beta ref}$ without a synchronization unit that is PLL. Moreover, it mitigates the active and reactive power oscillations under grid faults. The modelling of the DC-link voltage controller is discussed in section 5.2.1. A detailed discussion of APR with DRPS controller, APCMR controller and PCRCG are provided in section 5.3.

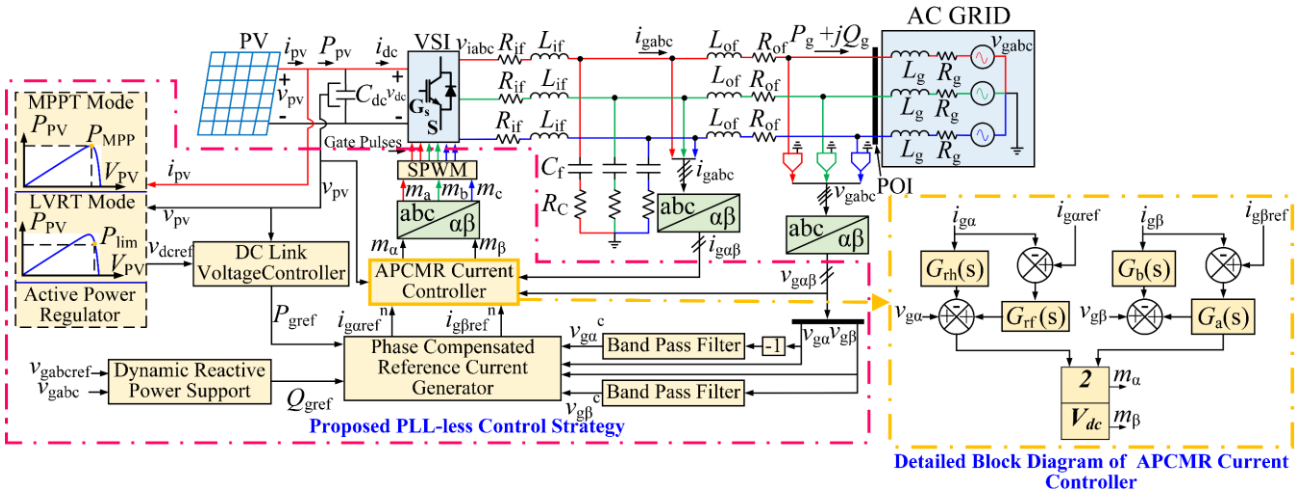

Fig. 5.1. Architecture of the proposed PLL-less control strategy with APCMR controller for grid-tied PV system.

5.2.1 DC-link Voltage Controller Design

The main objective of the DC-link voltage controller is to maintain constant voltage across the DC-link capacitor by controlling the active power injected into the grid. The block diagram of the DC-link voltage controller is shown in Fig. 5.2. The dynamics of the DC-

link voltage controller is based on power balance relationship of the DC-link capacitor. By neglecting the losses in the VSI, the power balance at the DC-link capacitor is given by

$$\left.\begin{aligned} P_{\mathrm{PV}} &= \frac{d}{dt}\left(\frac{1}{2}C_{\mathrm{dc}}{v_{\mathrm{dc}}}^{2}\right)+P_{\mathrm{g}} \\ P_{\mathrm{stored}} &= \frac{d}{dt}\left(\frac{1}{2}C_{\mathrm{dc}}{v_{\mathrm{dc}}}^{2}\right)=P_{\mathrm{PV}}-P_{\mathrm{g}} \end{aligned}\right\} \tag{5.1}$$

where C_{dc} is the DC-link capacitor and v_{dc} is the voltage across it. P_{stored}, P_{PV} and P_{g} are the power stored in the DC-link capacitor, PV array power and the active power injected to the grid. The P_{PV} is expressed as

$$P_{\mathrm{PV}} = v_{\mathrm{dc}} i_{\mathrm{dc}} = v_{\mathrm{PV}} i_{\mathrm{PV}} \tag{5.2}$$

where v_{PV}, i_{PV} and i_{dc} are the PV array voltage, PV array current and the current flowing in the DC side of the VSI. By substituting (5.2) in (5.1),

$$C_{\mathrm{dc}}\frac{dv_{\mathrm{dc}}}{dt} = i_{\mathrm{PV}} - \frac{P_{\mathrm{g}}}{v_{\mathrm{dc}}} \tag{5.3}$$

It can be noted that (5.3) is not in the form of a linear time-invariant (LTI) system. The nonlinearity in (5.3) is introduced by i_{pv}, which is a nonlinear function of v_{PV}. This expression can be linearized using a feedback linearization (FBL) technique. According to the FBL technique, (5.3) can be expressed as

$$C_{\mathrm{dc}}\frac{dv_{\mathrm{dc}}}{dt} = u_{\mathrm{dc}} \tag{5.4}$$

where u_{dc} is the new control input. The DC link voltage controller minimizes the steady state error in DC-link voltage and generates P_{gref} through a PI compensator $G_{\mathrm{c}}^{\mathrm{vdc}}$.

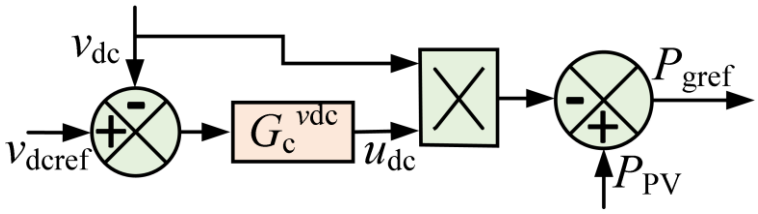

Fig.5.2. Block diagram of the DC-link voltage controller.

5.3 Proposed PLL-Less Control Strategy

The proposed APR, with DRPS controller integrated with APCMR controller is operated in a coordinated manner for simultaneous enhancement of LVRT capability under grid faults and suppression of grid current harmonics under distorted and weak grid conditions. Moreover, a PCRCG is incorporated with the proposed control strategy to mitigate the active and reactive power oscillations under unbalanced grid voltage faults. section 5.3.1

demonstrates the APR with DRPS controller for improving the LVRT capability of the grid-tied PV system. The APCMR controller for suppression of grid current harmonics is discussed in section 5.3.2. The PCRCG is described through a mathematical model in section 5.3.3.

5.3.1 Active Power Regulator with Dynamic Reactive Power Support Controller

The objective of the APR is to curtail the active power injected into the grid during grid faults. The curtailment of active power is required to limit the current value within a prescribed limit of the grid-tied PV system. The DRPS consists of a closed-loop system designed to generate the reference reactive power Q_{gref} injected into the grid, which is proportional to the value of large voltage sag due to grid fault in the system. Further, the DRPS is integrated with APR to inject Q_{gref} without reaching maximum apparent power. The integrated APR with the DRPS controller is operated in a coordinated manner to enhance the LVRT capability of the grid-tied PV system during grid faults. However, the PLL-less control strategy (discussed in chapter 4) cannot inject Q_{gref} into the grid. Therefore, the LVRT capability enchantment is not possible in this control strategy. The block diagram of APR with DRPS controller is shown in Fig. 5.3. The DRPS block contains a PI-based AC voltage controller. The PI controller compares the measured grid voltage v_{gabc} with the reference grid voltage $v_{gabcref}$ = 1 pu. and generates Q_{gref}. The APR with DRPS controller operates the grid-tied PV system in MPPT and LVRT modes according to the grid voltage conditions. As shown in Fig. 5.3, when the per-unit grid voltage v_g(pu) is in the range $0.9 < v_g(\text{pu}) < 1.1$, the fault signal S_f is 0 and the switch SW is in position 1, the grid-tied PV system operates in MPPT mode. On the other hand, when there is a grid fault $v_g(\text{pu}) < 0.9$, S_f becomes 1 and the SW is triggered to position 2, the grid-tied PV system is operated in LVRT mode. The v_g(pu) is calculated as $v_g(\text{pu}) = \sqrt{v_{g\alpha}{}^2 + v_{g\beta}{}^2} / v_b$. Fig. 5.4 shows how the grid-tied PV system is controlled in MPPT and LVRT modes.

i. Maximum Power Point Tracking (MPPT) Mode

The MPPT mode is enabled in the case of grid voltage within $0.9 < v_g(\text{pu}) < 1.1$. An adaptive step size incremental conductance (ASINC) MPPT algorithm is used to generate the PV voltage reference ($v_{pvref} = v_{dcref}$) for the DC-link voltage controller [106]. The ASINC MPPT algorithm is based on a variable voltage step V_{st}. The direction of the next voltage change is based on the slope dp/dv_{pv} of the power versus voltage characteristics of PV array. When the operating point is far from the MPP, the slope of the PV array is large, and consequently, the tracking time to reach the MPP is fast. On the other hand, if the operating point is nearer

to the MPP, the slope and voltage step size becomes small, and there are negligible oscillations in PV voltage at steady state. The voltage step size is expressed as

$$V_{st} = x\left|\frac{v_{PV}(k)i_{PV}(k) - v_{PV}(k-1)i_{PV}(k-1)}{v_{PV}(k) - v_{PV}(k-1)}\right| \tag{5.5}$$

where v_{pv}(k), i_{pv}(k), v_{pv}(k-1) and i_{pv}(k-1) are PV voltages and currents at k th and (k-1) th iteration. x is the scaling coefficient of the MPPT controller to adjust the step size. The DC-link voltage controller generates active reference power P_{gref} by comparing v_{dcref} with the measured v_{dc} (equal to v_{pv}). Further, the reactive power reference Q_{gref} from the DRPS is zero as the error between v_{gabc} and $v_{gabcref}$ is zero.

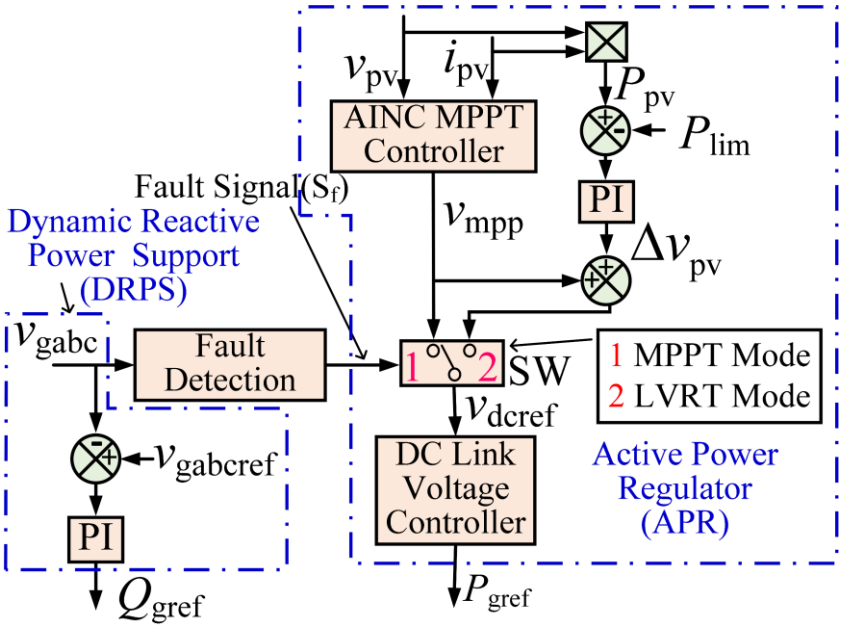

Fig. 5.3. Block diagram of the APR with DRPS controller.

ii. Low Voltage Ride Through (LVRT) Mode

The LVRT mode is triggered, when a fault occurs at the POI and the v_g(pu) <0.9. In this mode, the flexible power point tracking (FPPT) controller based on the ASINC MPPT algorithm is used to enhance the LVRT capability of the grid-tied PV system. The FPPT controller reduces P_{pv} to a limited value P_{lim} during grid faults to provide reactive power injection capability based on the grid code. To decrease P_{pv}, the FPPT controller ceases the MPP operation at V_{LVRT} and controls the P_{pv} to match the active power to be injected into the grid. Therefore, the PV characteristics operating point moves from A to B as shown in Fig. 5.4. A PI controller is used to achieve this, which generates step voltage Δv_{pv} to be added to the V_{MPP}. The new operating point V_{LVRT} is expressed as

$$V_{LVRT} = V_{MPP} + \Delta v_{pv} \tag{5.6}$$

The input of the PI controller is the error between P_{PV} and P_{lim}. It is noted that Δv_{pv} is added to the V_{MPP} only during grid faults, and it is disconnected during normal operations of the grid-tied PV system. The grid-tied PV system operation under MPPT mode and LVRT mode is summarized in Table 5.1.

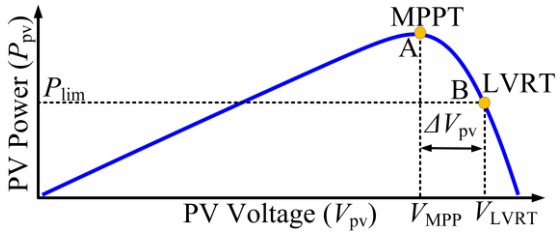

Fig. 5.4 PV characteristics when the grid-tied PV system switches between MPPT and LVRT mode.

Table 5.1. Grid-tied PV System Operation Under Different Grid Condition's

Grid Conditions	Fault signal (S_f)	Operating mode of grid-tied PV system
0.9 < v_g(pu)< 1.1	Disabled	MPPT
v_g(pu)< 0.9	Enabled	LVRT

5.3.2 Proposed Advanced Phase Compensated Multiresonant Controller

In the conventional proportional multi-resonant controller (CPMR), the phase margin and the bandwidth of the grid-tied PV system decreases, and one of the poles generated by the CPMR moves towards the right half-plane with the increase of grid impedance Z_g under weak grid conditions. Also, the CPMR controller has infinite gain and narrower band width due to the high gain frequency slope at the resonant frequency [128]. Thus, the implementation of the CPMR controller is challenging. Moreover, the CPMR controller makes the grid-tied PV system unstable, and thus it is unable to reduce grid current harmonics under the weak grid and heavily distorted grid voltage conditions.

To take care of these issues, in the proposed APCMR controller, a phase leading angle is added at the resonant frequency to increase the system's phase margin and band width for improving of the performance of grid-tied PV system under weak grid conditions. The objective of the APCMR current controller is to maintain the grid current quality of the grid-tied PV system in the case of the weak grid and distorted grid voltage conditions. Fig. 5.5 shows the control structure block diagram of the APCMR current controller, which consists of two parallel branches with phase compensation angle in their transfer functions. The first branch is called the proportional resonant controller (PRC) with transfer function G_{rf}(s) to track the fundamental grid current of the grid-tied PV system. The second branch consists of multiple resonant harmonic controllers (RHC) with transfer function G_{rh}(s) to mitigate the current harmonics. The transfer function of G_{rf} (s) and G_{rh}(s) are expressed as

$$\left.\begin{aligned} G_{\mathrm{rf}}(s) &= \frac{k_{\mathrm{r}} 2\xi\omega_{\mathrm{g}}\left\{s\cos(\theta_1)-\omega_{\mathrm{g}}\sin(\theta_1)\right\}}{s^2+2\xi\omega_{\mathrm{g}}s+\omega_{\mathrm{g}}{}^2}; \\ G_{\mathrm{rh}}(s) &= k_p + \sum_{h=5,7,11,\ldots}^{n} \frac{k_{\mathrm{rh}} 2\xi(h\omega_{\mathrm{g}})\left\{s\cos(\theta_h)-(h\omega_{\mathrm{g}})\sin(\theta_h)\right\}}{s^2+2\xi(h\omega_g)s+(h\omega_g)^2}; \\ \theta_{\mathrm{h}} &= \frac{\pi}{4}-2\tan^{-1}\sqrt{\frac{K_p}{K_p+K_{rh}}}. \end{aligned}\right\} \tag{5.7}$$

where k_{p}, k_{r} and k_{rh} are the proportional coefficient, fundamental resonant coefficient and resonant coefficients at the order h of the APCMR controller. θ_{h} is the phase compensation angle at the selected harmonic frequency $h\omega_g$. ξ, h and ω_{g} are the damping factor, harmonic order and grid fundamental resonant frequency, respectively.

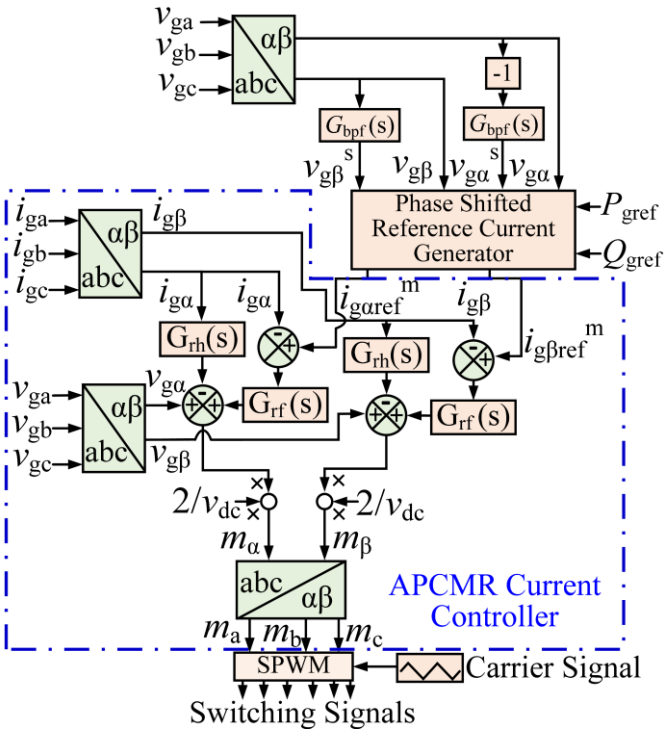

Fig. 5.5. Control schematic of the proposed advanced phase compensated multi resonant controllers

It is observed from Fig. 5.5 that the grid current reference signals $i_{g\propto ref}{}^{m}$ and $i_{g\beta ref}{}^{m}$ are obtained from the output of the PCRCG. Further, the output of the proposed APCMR current controller is given to a SPWM module to generate the gating signals for the IGBTs of the VSI. Fig. 5.6 shows the detailed implementation steps of the proposed PLL-less control strategy.

5.3.2.1 Frequency Response Analysis of the Proposed APCMR Controller

To evaluate the improved performance of the proposed APCMR controller for suppressing the grid current harmonics, the frequency responses of the open-loop and closed-loop current control transfer functions are investigated in this section. Moreover, the effect of

variable grid impedance Z_g on the frequency response of the APCMR is provided to consider the weak grid condition. The simplified equivalent circuit of a grid tied VSI is shown in Fig. 5.7, where Z_{if}, and Z_{of} denote the series impedances of filter at the inverter side and at the grid side; Z_c and Z_g are shunt impedance of the filter and equivalent grid impedance. The VSI output voltage is expressed as

$$v_{i\alpha\beta} = \frac{v_{dc}}{2} m_{\alpha\beta} \tag{5.8}$$

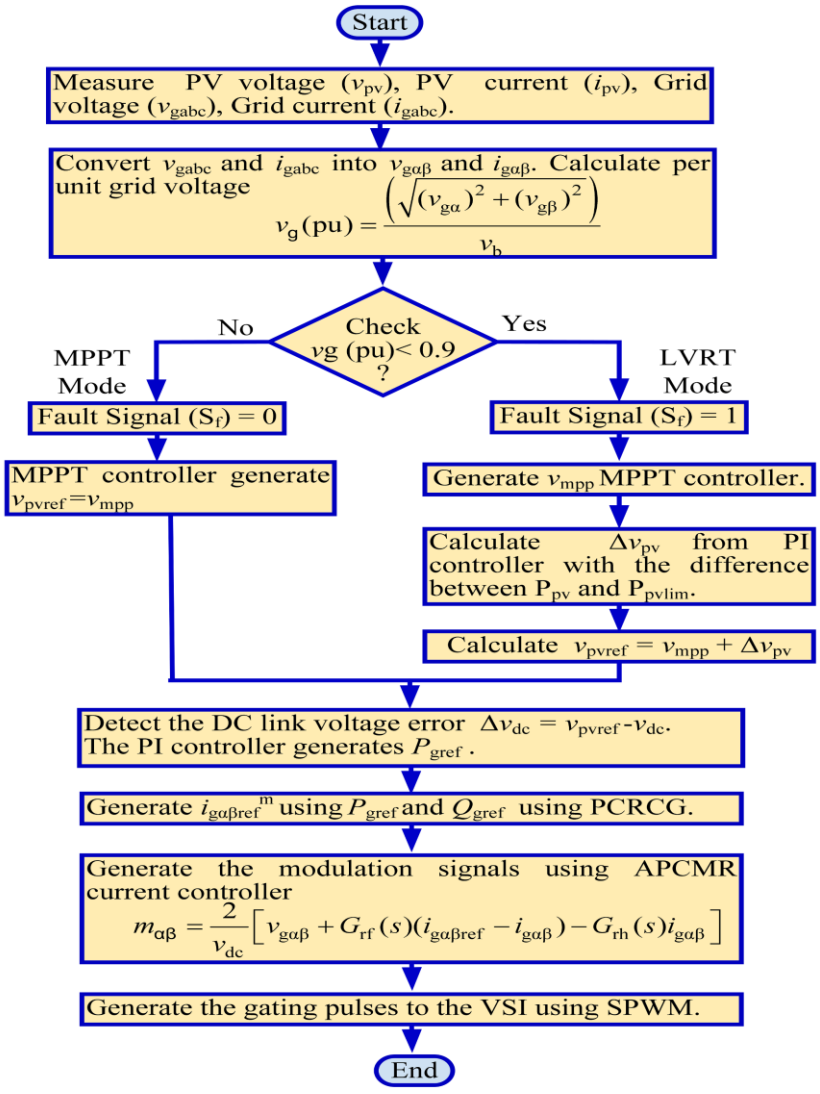

Fig. 5.6. Implementation steps of the proposed PLL-less control strategy.

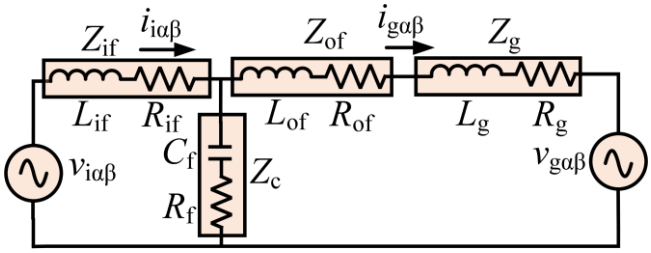

Fig. 5.7. Simplified equivalent circuit of the grid-tied VSI.

where $v_{i\alpha\beta}$ is the inverter output voltage in $\alpha\beta$ reference frame, v_{dc} is DC-link voltage and $m_{\propto\beta}$ is the modulation signal of the VSI obtained from the output of the APCMR controller. The modulation signal of the VSI can be obtained from Fig. 5.5 as follows

$$m_{\alpha\beta} = \frac{2}{v_{dc}}\left[G_{rf}(s) i_{g\alpha\beta ref}{}^{m} - \left\{ G_{rf}(s) + G_{rh}(s) \right\} i_{g\alpha\beta} + v_{g\alpha\beta} \right]. \tag{5.9}$$

From (5.8) and Fig. 5.7, the grid voltage $v_{g\alpha\beta}$, inverter voltage $v_{i\alpha\beta}$ and the inverter current $i_{i\alpha\beta}$ can be derived as

$$\left.\begin{aligned} v_{g\alpha\beta} &= \frac{v_{i\alpha\beta}}{2} - Z_{if}(s) i_{i\alpha\beta} - \left\{ Z_g(s) + Z_{of}(s) \right\} i_{g\alpha\beta} \\ i_{i\alpha\beta} &= \left(\frac{\left\{ Z_{of}(s) + Z_g(s) \right\} i_{g\alpha\beta} + v_{g\alpha\beta}}{Z_c(s)} \right) + i_{g\alpha\beta} \\ v_{i\alpha\beta} &= \frac{2}{m_{\alpha\beta}} \left(Z_{if}(s) i_{i\alpha\beta} + Z_c(s)(i_{i\alpha\beta} - i_{g\alpha\beta}) \right) \end{aligned}\right\} \tag{5.10}$$

By substituting (5.10) in (5.9), the open-loop transfer function $G_{ol}(s)$ and the closed-loop transfer function $G_{ig\text{-}cl}(s)$ from $i_{g\alpha\beta ref}{}^{m}$ to $i_{g\alpha\beta}$ can be derived as

$$G_{ol}(s) = \frac{\left\{ Z_{cf}(s) + Z_{of}(s) + Z_g(s) \right\} \left\{ G_{rf}(s) + G_{rh}(s) \right\}}{Z_{if}(s) \left\{ Z_{cf}(s) + Z_{of}(s) + Z_g(s) \right\} + Z_{cf}(s) \left\{ Z_{of}(s) + Z_g(s) \right\}} \tag{5.11}$$

$$G_{i_g\text{-}cl}(s) = \frac{i_{g\alpha\beta ref}{}^{m}}{i_{g\alpha\beta}} = \frac{Z_c(s) G_{rf}(s)}{\begin{aligned} &\left[Z_c(s) + \left\{ Z_{of}(s) + Z_g(s) \right\} \left\{ G_{rf}(s) + G_{rh}(s) \right\} \right] + \\ &\left[Z_{if}(s) Z_c(s) + Z_c(s) \left\{ Z_{of}(s) + Z_g(s) \right\} \right] + \\ &Z_{if}(s) \left\{ Z_{of}(s) + Z_g(s) \right\} \end{aligned}} \tag{5.12}$$

In order to investigate the impact of variations on grid inductance L_g, the Bode diagrams of the open-loop transfer function $G_{ol}(s)$ of the APCMR controller with L_g = 2 mH, 6 mH and 10 mH are presented in Fig. 5.8. As shown in Fig. 5.8(a), increasing L_g results in slight decrease in the magnitude of $G_{ol}(s)$ at the fundamental frequency 50 Hz and selective harmonic frequencies 250 Hz, 350 Hz, 550 Hz, 650 Hz, 850 Hz and 950 Hz. However, such a drop in magnitude does not affect the stability of the grid-tied PV system adversely. As demonstrated in Fig. 5.8(b), the phase margin is positive and still sufficient (42.3°, 36.5°, and 33° for L_g = 2 mH, 6 mH and 10 mH, respectively). Therefore, it can be concluded that variation in the grid impedance does not affect the control performance of the proposed APCMR controller. The Bode diagram of closed-loop transfer function $G_{ig\text{-}cl}(s)$ of the APCMR controller with different ξ and θ_h are shown in Fig. 5.9. The Bode diagram of $G_{ig\text{-}cl}(s)$ with K_p= 80, K_{rf} = 240, K_{rh} = 240 with variable ξ is shown in Fig. 5.9(a). It is seen that

when the value of ξ increases, the magnitude of $G_{ig\text{-}cl}(s)$ has a flat top at 50 Hz and also has a minimal negative peak at the specified harmonic frequencies. Hence the grid current harmonics are eliminated at lower values of ξ. Thus, a small value of ξ is selected to attenuate the grid current harmonics. As seen from Fig. 5.9(b), with the increase in θ_h, the phase at fundamental grid frequency (50 Hz) increases. Also, a larger θ_h increases the magnitude of $G_{ig\text{-}cl}(s)$ at fundamental grid frequency (50 Hz) and decreases the magnitude at selected harmonic frequencies. Therefore, a higher value of θ_h is preferred to ensure zero steady-state error of the grid current and suppression of grid current harmonics.

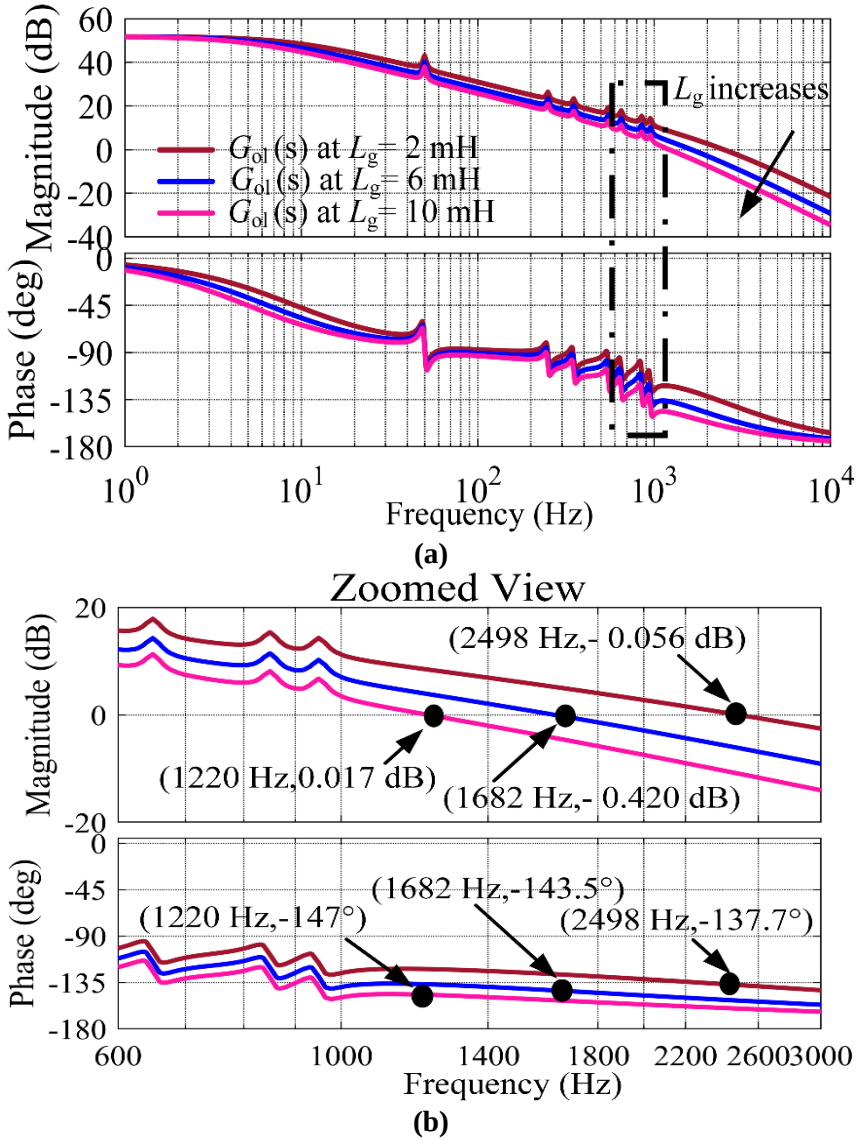

Fig. 5.8. Bode diagram of the open-loop transfer function $G_{ol}(s)$ of the APCMR controller with grid inductance variation **(a)** Full scale **(b)** Zoomed in figure.

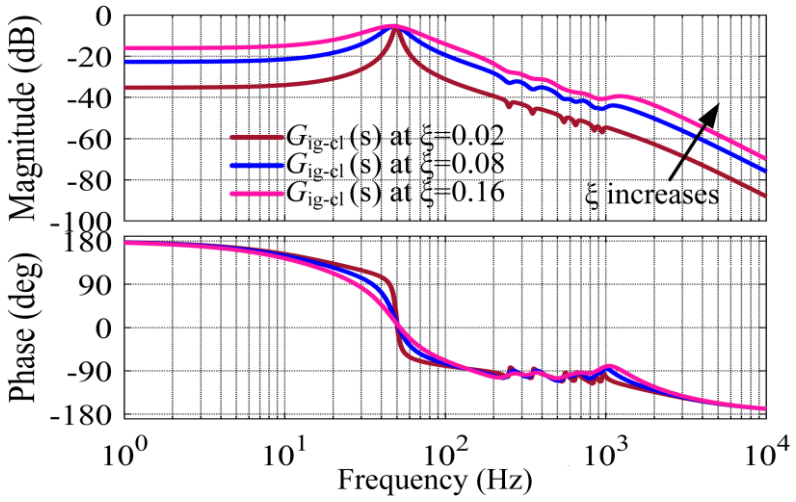

(a)

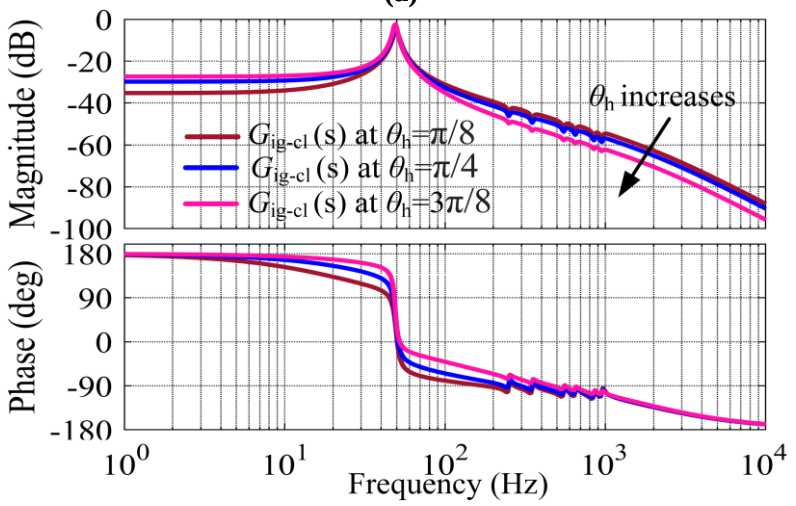

(b)

Fig. 5.9. Bode diagram of the closed loop transfer function $G_{ig\text{-}cl}(s)$ (a) for different values of ξ with K_p= 80, K_{rf} = 240 K_{rh} = 240. (b) for different values of θ_h with K_p= 80, K_{rf}= 240, K_{rh}=240, and ξ = 0.02.

The Bode diagram of G_{rf} (s), $G_{rh}(s)$ and $G_{ig\text{-}cl}$ (s) of the APCMR controller is shown in Fig. 5.10. It is seen from Fig. 5.10(a) that the magnitude of G_{rf} (s) is approximately 50 dB at resonant frequency (50Hz). Moreover, there are peaks which are appearing in $G_{rh}(s)$ at the selected harmonics frequencies 250 Hz, 350 Hz, 550 Hz,650 Hz, 850 Hz, and 950 Hz. The selected current harmonics are reduced, as the output of $G_{rh}(s)$ is subtracted from the output of $G_{rf}(s)$ as seen in Fig. 5.5. As a result, the modulating signal m_{abc} obtained at the output of the proposed APCMR controller contains reduced magnitude of selected harmonics. As seen from Fig. 5.10(b), the magnitude of $G_{ig\text{-}cl}$ (s) at the resonant frequency is 0 dB (unity gain) with a phase shift of 0°. Consequently, the steady-state error in the fundamental component of the grid current becomes zero. Also, it is observed that the magnitude of $G_{ig\text{-}cl}$ (s) has negative peaks and attenuated at the selected frequencies. Therefore, the proposed APCMR controller suppresses the grid current harmonics.

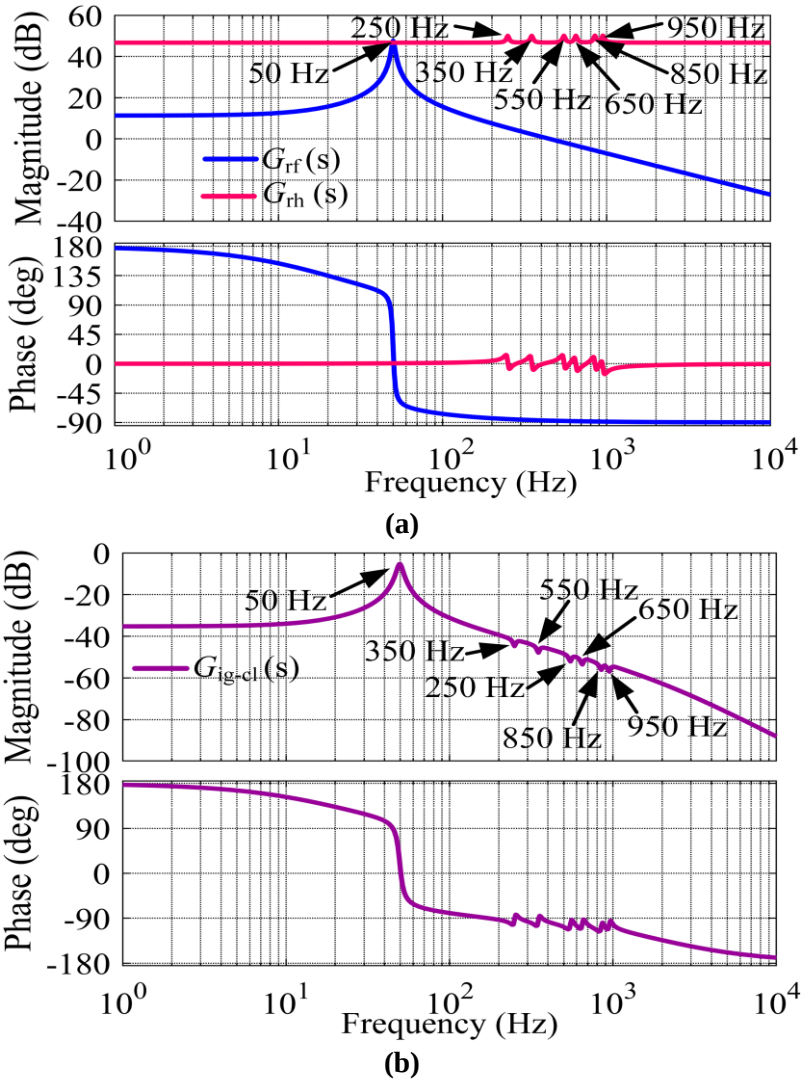

Fig. 5.10. Bode diagram of (a) G_{rf} (s) and G_{rh}(s) of the APCMR controller (b) $G_{ig\text{-}cl}$ (s) of the APCMR controller with $K_p = 80$, $K_{rf} = 240$ $K_{rh} = 240$ and $\xi = 0.02$.

5.3.3 Phase Compensated Reference Current Generator

Asymmetrical grid fault is a critical scenario for the grid-tied PV system due to the unbalanced power flow in the three phases. Under these conditions, the positive and negative sequence voltage vectors in $\alpha\beta$ reference frame is expressed as

$$\begin{bmatrix} v_{g\alpha} \\ v_{g\beta} \end{bmatrix} = \begin{bmatrix} v_{g\alpha}^{+} \\ v_{g\beta}^{+} \end{bmatrix} + \begin{bmatrix} v_{g\alpha}^{-} \\ v_{g\beta}^{-} \end{bmatrix} = \begin{bmatrix} V_p \sin(\omega t + \delta_p) \\ -V_p \cos(\omega t + \delta_p) \end{bmatrix} + \begin{bmatrix} V_n \sin(\omega t + \delta_n) \\ V_n \cos(\omega t + \delta_n) \end{bmatrix} \tag{4.13}$$

where $v_{g\alpha}^{+}$, $v_{g\alpha}^{-}$, $v_{g\beta}^{+}$ and $v_{g\beta}^{-}$ are the positive and negative sequence components of $v_{g\alpha}$ and $v_{g\beta}$ in $\alpha\beta$ reference frame, respectively. V_p and V_n represent the positive and negative sequences voltage magnitudes; δ_p and δ_n represent the positive and negative sequence phase angles and ω is the angular frequency, respectively.

The instantaneous active power P_g and reactive power Q_g injected to the grid is expressed as

$$\begin{bmatrix} P_g \\ Q_g \end{bmatrix} = \frac{3}{2}\begin{bmatrix} v_{g\alpha} & v_{g\beta} \\ v_{g\beta} & -v_{g\alpha} \end{bmatrix}\begin{bmatrix} i_{g\alpha} \\ i_{g\beta} \end{bmatrix} \tag{5.14}$$

The reference current value $i_{g\alpha ref}$ and $i_{g\beta ref}$ based on the P_{gref}, Q_{gref}, $v_{g\propto}$ and $v_{g\beta}$ can be derived from (5.14). $i_{g\alpha ref}$ and $i_{g\beta ref}$ have four vectors of positive and negative sequences and active and reactive component. These components are expressed as

$$\left.\begin{aligned} \begin{bmatrix} i_{g\alpha ref} \\ i_{g\beta ref} \end{bmatrix} &= \begin{bmatrix} i_{g\alpha ref(p)} \\ i_{g\beta ref(p)} \end{bmatrix} + \begin{bmatrix} i_{g\alpha ref(q)} \\ i_{g\beta ref(q)} \end{bmatrix} \\ &= \begin{bmatrix} I_p \sin(\omega t+\delta_p) + I_n \sin(\omega t+\delta_n) \\ -I_p \cos(\omega t+\delta_p) + I_n \cos(\omega t+\delta_n) \end{bmatrix} + \begin{bmatrix} -I_p \cos(\omega t+\delta_p) + I_n \cos(\omega t+\delta_n) \\ -I_p \sin(\omega t+\delta_p) - I_n \sin(\omega t+\delta_n) \end{bmatrix} \end{aligned}\right\} \tag{5.15}$$

where I_p and I_n represent the positive and negative sequence current magnitudes.

By substituting (5.15) in (5.14), the active power P_{gosc} injected into the grid is calculated by considering $i_{g\propto ref(p)}$ and $i_{g\beta ref(p)}$, whereas the reactive power Q_{gosc} is calculated by considering $i_{g\propto ref(q)}$ and $i_{g\beta ref(q)}$. The P_{gosc} and Q_{gosc} are expressed as

$$\left.\begin{aligned} P_{gosc} &= \frac{P_{gref}}{(V_p)^2+(V_n)^2}\left[(v_{g\alpha})^2+(v_{g\beta})^2\right] \\ &= P_{gref} - \frac{2P_{gref}V_pV_n}{(V_p)^2+(V_n)^2}\cos(2\omega t+\delta_p+\delta_n) = P_{gref}+P_{g2\omega} \\ Q_{gosc} &= \frac{Q_{gref}}{(V_p)^2+(V_n)^2}\left[(v_{g\alpha})^2+(v_{g\beta})^2\right] \\ &= Q_{gref} - \frac{2Q_{gref}V_pV_n}{(V_p)^2+(V_n)^2}\cos(2\omega t+\delta_p+\delta_n) = Q_{gref}+Q_{g2\omega} \end{aligned}\right\} \tag{5.16}$$

It is observed from (5.16) that P_{gosc} and Q_{gosc} have double grid frequency oscillations. These oscillations are due to oscillating terms of $\cos(2\omega t+\delta_p+\delta_n)$. These power oscillations cause significant DC-link voltage oscillations. The oscillation in DC-link voltage is written as

$$v_{dc2\omega} = \frac{P_{g2\omega}}{\omega C_{dc} V_{dc}} \tag{5.17}$$

where $v_{dc2\omega}$ and $P_{g2\omega}$ are the magnitudes of the second-order oscillating DC-link voltage and oscillating active power. C_{dc} is the DC-link capacitor with DC-link voltage v_{dc}.

The oscillations in DC-link voltage shorten the life cycle of the DC-link capacitor and PV panels of the grid-tied PV system. These oscillations also reduce the power efficiency of the PV array and deteriorates the power quality of the grid-tied PV system. Further, the oscillations in reactive power increase the grid current, which results into increase in losses in the grid-tied PV system.

To take care of the above issues during grid faults, a phase-compensated reference current generator (PCRCG) is presented in this work. The salient features of the PCRCG are:

i) It eliminates the PLL block of the grid-tied PV system by generating the reference grid currents $i_{g\alpha ref}$ and $i_{g\beta ref}$ for the APCMR current controller by utilizing the grid injected active power P_g, reactive power Q_g, and grid voltages $v_{g\alpha}$ and $v_{g\beta}$ to realize self-synchronization.

ii) It eliminates the active and reactive power oscillations as well as DC-link voltage oscillations during grid faults.

The block diagram of the PCRCG is illustrated in Fig. 5.11. The PCRCG is an improved version of the current reference generator (RCG), and it eliminates the active and reactive power oscillations by introducing a phase shift in $\alpha\beta$ component of the grid voltages $v_{g\alpha}$ and $v_{g\beta}$. This phase shift in the grid voltages is obtained by a bandpass filter. The PCRCG is used to generate $i_{g\alpha ref}$ and $i_{g\beta ref}$ for the APCMR current controller. Further, the PCRCG and APCMR controller are integrated and embedded into a compact and simple structure; thus, the need for PLL is avoided. As a result, the proposed control strategy synchronizes the VSI to the grid without any PLL unit and makes the grid-tied PV system self-synchronized.

The reference active power P_{gref} and reactive power Q_{gref} can be expressed as.

$$\begin{bmatrix} P_{gref} \\ Q_{gref} \end{bmatrix} = \frac{3}{2}\begin{bmatrix} v_{g\alpha} & v_{g\beta} \\ -v_{g\alpha}G_{bpf}(s) & v_{g\beta}G_{bpf}(s) \end{bmatrix}\begin{bmatrix} i_{g\alpha ref}{}^{m} \\ i_{g\beta ref}{}^{m} \end{bmatrix} = \frac{3}{2}\begin{bmatrix} v_{g\alpha} & v_{g\beta} \\ v_{g\alpha}{}^{s} & -v_{g\beta}{}^{s} \end{bmatrix}\begin{bmatrix} i_{g\alpha ref}{}^{m} \\ i_{g\beta ref}{}^{m} \end{bmatrix} \tag{5.18}$$

where $v_{g\propto}{}^{s}$ and $v_{g\beta}{}^{s}$ are the α and β grid voltage components shifted by 135° and 45° phase angle in $v_{g\propto}$ and, $v_{g\beta}$. $i_{g\propto ref}{}^{m}$ and $i_{g\beta ref}{}^{m}$ are the α and β compensated grid current references. $G_{bpf}(s)$ is the transfer function of band pass filter and used for the phase compensation in $v_{g\propto}$ and $v_{g\beta}$. The transfer function of band pass filter $G_{bpf}(s)$ is expressed as

$$G_{bpf}(s) = \frac{2\omega_c s}{s^2 + 2\omega_c s + \omega_o{}^2} \tag{5.19}$$

where ω_c and ω_o indicate the resonance bandwidth and the resonance frequency of the BPF ($\omega_c = \alpha\omega_o$). In this work, the value of ω_o is set as the grid frequency (ω_o = 314.15 rad/sec). α is set at 1.

The $v_{g\propto}$ is passed through the bandpass filter for achieving a phase compensation of 135° in $v_{g\propto}$ by $-G_{bpf}(s)$ and $v_{g\beta}$ is passed through the bandpass filter by achieving are 45° in $v_{g\beta}$ by $G_{bpf}(s)$. As a consequence, twice of the grid frequency oscillations in active and reactive powers are eliminated.

The phase-shifted grid voltage $v_{g\propto}{}^{s}$ and $v_{g\beta}{}^{s}$ can be expressed as

$$\begin{bmatrix} v_{g\alpha}{}^{s} \\ v_{g\beta}{}^{s} \end{bmatrix} = \begin{bmatrix} V_{p}\sin(\omega t + \delta_{p} - 135) \\ -V_{p}\cos(\omega t + \delta_{p} + 45) \end{bmatrix} + \begin{bmatrix} V_{n}\sin(\omega t + \delta_{n} - 135) \\ V_{n}\cos(\omega t + \delta_{n} + 45) \end{bmatrix} \tag{5.20}$$

The compensated injected current reference $i_{g\propto ref}{}^{m}$ and $i_{g\beta ref}{}^{m}$ due to phase shift in grid voltages $v_{g\propto}$ and $v_{g\beta}$ are obtained from (5.18) as follows

$$\begin{bmatrix} i_{g\alpha ref}{}^{m} \\ i_{g\beta ref}{}^{m} \end{bmatrix} = \frac{2}{3}\begin{bmatrix} v_{g\alpha} & v_{g\beta} \\ v_{g\alpha}{}^{s} & -v_{g\beta}{}^{s} \end{bmatrix}^{-1}\begin{bmatrix} P_{gref} \\ Q_{gref} \end{bmatrix} = \begin{bmatrix} i_{g\alpha ref\,(p)}{}^{m} + i_{g\alpha ref\,(q)}{}^{m} \\ i_{g\beta ref\,(p)}{}^{m} + i_{g\beta ref\,(q)}{}^{m} \end{bmatrix} \tag{5.21}$$

$$\left.\begin{aligned} i_{g\alpha ref\,(p)}{}^{m} &= \frac{2}{3}\frac{P_{gref}v_{g\beta}{}^{s}}{v_{g\alpha}v_{g\beta}{}^{s} + v_{g\alpha}{}^{s}v_{g\beta}} = \frac{2}{3}\frac{P_{gref}v_{g\beta}{}^{s}}{(V_{p})^{2} - (V_{n})^{2}} \\ i_{g\alpha ref\,(q)}{}^{m} &= \frac{2}{3}\frac{Q_{gref}v_{g\beta}}{v_{g\alpha}v_{g\beta}{}^{s} + v_{g\alpha}{}^{s}v_{g\beta}} = \frac{2}{3}\frac{Q_{gref}v_{g\beta}}{(V_{p})^{2} - (V_{n})^{2}} \\ i_{g\beta ref\,(p)}{}^{m} &= \frac{2}{3}\frac{P_{gref}v_{g\alpha}{}^{s}}{v_{g\alpha}v_{g\beta}{}^{s} + v_{g\alpha}{}^{s}v_{g\beta}} = \frac{2}{3}\frac{P_{gref}v_{g\alpha}{}^{s}}{(V_{p})^{2} - (V_{n})^{2}} \\ i_{g\beta ref\,(q)}{}^{m} &= -\frac{2}{3}\frac{Q_{gref}v_{g\alpha}}{v_{g\alpha}v_{g\beta}{}^{s} + v_{g\alpha}{}^{s}v_{g\beta}} = \frac{2}{3}\frac{Q_{gref}v_{g\alpha}}{(V_{p})^{2} - (V_{n})^{2}} \end{aligned}\right\} \tag{5.22}$$

The modified active and reactive powers are written as

$$\begin{bmatrix} P_{g\,mod} \\ Q_{g\,mod} \end{bmatrix} = \frac{3}{2}\begin{bmatrix} v_{g\alpha} & v_{g\beta} \\ v_{g\alpha}{}^{s} & -v_{g\beta}{}^{s} \end{bmatrix}\begin{bmatrix} i_{g\alpha ref}{}^{m} \\ i_{g\beta ref}{}^{m} \end{bmatrix} \tag{5.23}$$

By substituting (5.21) in (5.22,) the modified active and reactive powers can be expressed as

$$\left.\begin{aligned} P_{g\,mod} &= P_{gref}\left[\frac{v_{g\alpha}v_{g\beta}{}^{s} + v_{g\alpha}{}^{s}v_{g\beta}}{(V_{p})^{2} - (V_{n})^{2}}\right] = P_{gref}\frac{(V_{p})^{2} - (V_{n})^{2}}{(V_{p})^{2} - (V_{n})^{2}} \\ Q_{g\,mod} &= Q_{gref}\left[\frac{v_{g\alpha}{}^{s}v_{g\beta} - v_{g\alpha}v_{g\beta}{}^{s}}{(V_{p})^{2} - (V_{n})^{2}}\right] = Q_{gref}\frac{(V_{p})^{2} - (V_{n})^{2}}{(V_{p})^{2} - (V_{n})^{2}} \end{aligned}\right\} \tag{5.24}$$

According to (5.23), there is no oscillations terms of $\cos(2\omega t+\delta_{p}+\delta_{n})$ in P_{gmod} and Q_{gmod}. As a result, the PCRCG minimizes the active and reactive power oscillations caused by asymmetrical grid faults. Moreover, because oscillations in P_{gmod} are reduced, the DC-link voltage oscillations are also reduced. The reduction of power oscillations has various advantages in the grid-tied PV system, including increased power efficiency of the PV array, reduced power losses and increased life span of DC-link capacitors and PV panels.

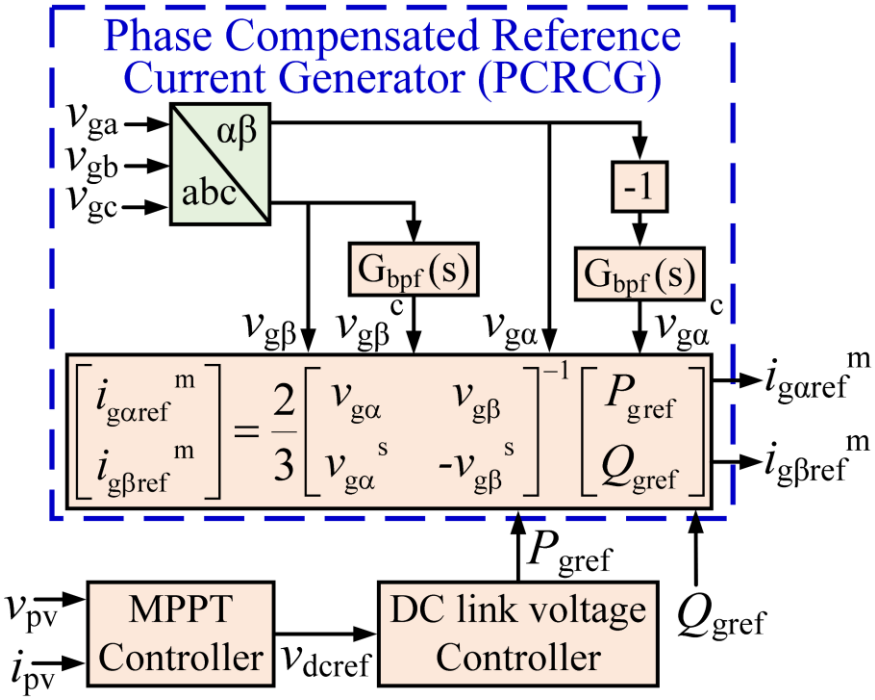

Fig. 5.11. Block diagram of the phase-compensated reference current generator.

5.4 Experimental Verifications

An experimental setup of 4.3 kW grid-tied PV system has been developed in the laboratory as shown in Fig. 5.12. The system and control parameters of the grid-tied PV system are presented in Table 5.2. The detailed experimental studies are carried out to demonstrate the effectiveness and feasibility of the proposed PLL-less control strategy. The proposed control strategy is implemented with the help of OPAL-RT OP4510 real-time digital simulator using the current and voltage signals obtained through current sensors LA-55P and voltage sensors LV-25P. The Chroma 62050H-600S programmable DC source is used in this experiment setup as a PV simulator and connected to the grid simulator ITEC GS010 415-16 through VSI and LCL filter. The switching signals of IGBT modules for the Semikron SKM 150-GB 12T4 VSI are taken from the digital I/O of OPAL-RT and fed through Skyper-32 gate drivers. The performance of the grid-tied PV system has been evaluated under adverse grid conditions, such as under harmonically distorted grid voltages, variable grid impedances, various grid faults and grid frequency variations. Further, the effectiveness of the proposed PLL-less control strategy (PLCS) with APCMR controller is compared with conventional PLL-based control strategy (PBCS) with CPMR controller.

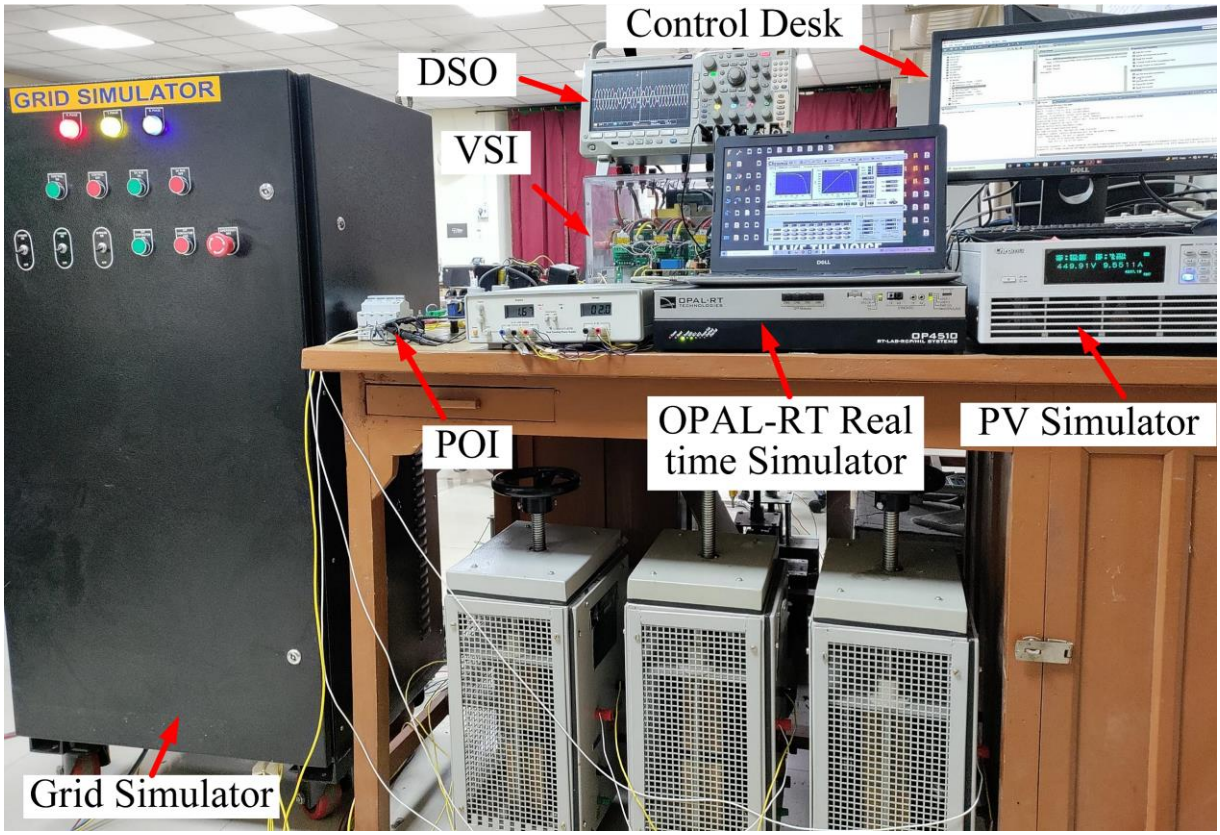

Fig. 5.12. Photograph of the laboratory prototype.

Table 5.2. Real-time System and Control Parameters

	Description	Symbol	Value
System Parameters	Grid voltage amplitude	V_g	120 V (L-L rms)
	Grid frequency	f_g	50 Hz
	Switching frequency	f_s	10 kHz
	Grid inductance	L_g	2 mH, (10 mH Weak grid)
	Inverter side impedance	L_{if} , R_{if}	4.8 mH,0.037 Ω
	Filter capacitance	C_f	10 µF
	Grid side impedance	$L_{of,}$ R_{of}	1.2 mH, 0.016 Ω
	DC link capacitance	C_{dc}	4700 µF
	PV open circuit voltage	V_{PVoc}	530.0 V
	PV short circuit current	I_{PVsc}	10.25 A
	PV MPP voltage	V_{MPP}	450.0 V
	PV MPP current	I_{MPP}	9.56 A
	PV Maximum power	P_{MPP}	4.30 kW
Control Parameters	PI controller (DC-link voltage controller)	K_{pvdc} , K_{ivdc}	2, 30
	APMR controller	K_p, K_{rf}, K_{rh}, ξ	80, 240, 240, 0.02

5.4.1 Performance Evaluation Under Harmonically Distorted Grid Voltages

This section demonstrates the effectiveness of the proposed PLCS with APCMR controller under harmonically distorted grid voltages. The grid voltage is distorted by injecting 5^{th}, 7^{th}, 11^{th}, 13^{th}, 17^{th} and 19^{th} harmonics, and the magnitude of the harmonic component with respect to the fundamental grid voltage are 8%, 8%, 5%, 5%, 2% and 2% respectively. The dynamic experimental waveforms of grid voltages and grid currents are shown in Fig. 5.13. It is seen from Fig. 5.13(b) that the grid currents obtained by the conventional PBCS with CPMR controller are highly distorted. However, it is observed from Fig.5.13(c) that with the proposed PLCS with APCMR controller, the current distortions reduce and the grid currents became balanced and sinusoidal. It is observed from Fig. 5.13(b) that the THD of the grid current obtained by using the conventional PBCS with CPMR controller is 9.06%, which is above the stipulated limit of IEEE 519 standards [125]. However, the grid current THD is reduced to 2.84% using the proposed PLCS with APCMR controller. Further, as shown in Fig. 5.13(a), a single-phase grid voltage sag of 40% occurs in phase *a* of the grid voltage at t = t1. It is observed from Figs. 5.13(b) and (c) that the grid current is increased after *t*1 to maintain constant power operation. Further, the grid current is closer to sinusoidal and balanced using the proposed PLCS with APCMR controller as compared to the conventional PBCS with CPMR controller. Therefore, it is concluded that the proposed PLCS with APCMR controller enhances the current harmonic suppression capability of the grid-tied PV system under distorted grid voltages.

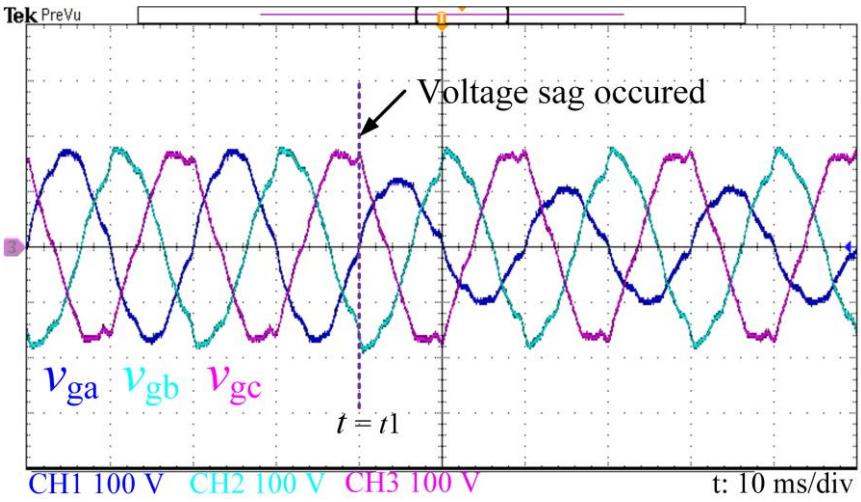

(a)

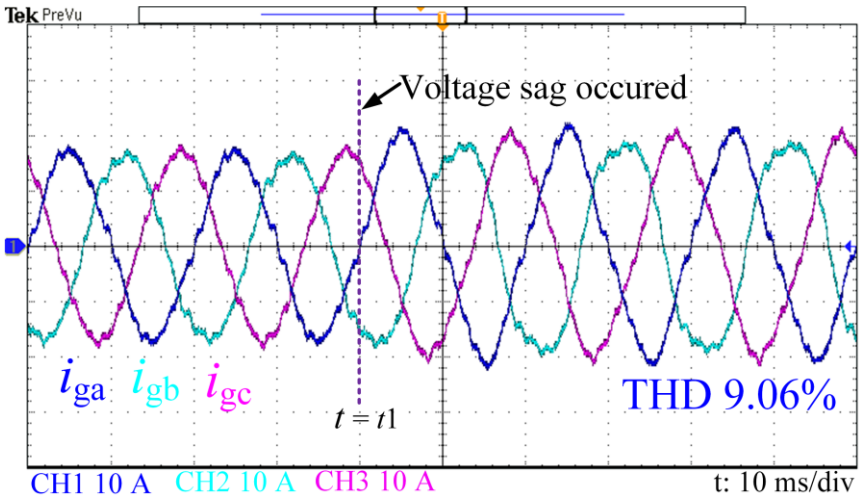

(b)

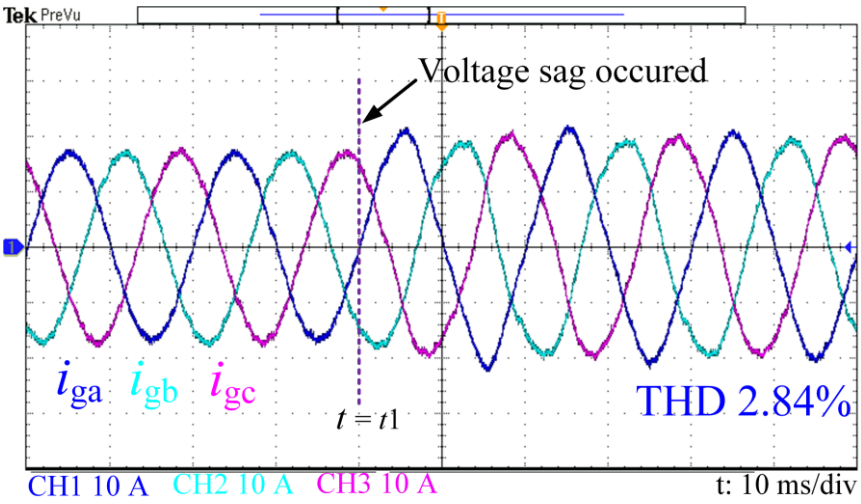

(c)

Fig. 5.13 Dynamic experimental waveforms under harmonically distorted grid voltages. (a)grid voltages. (b)grid currents obtained by using conventional PBCS with CPMR controller. (c) grid currents obtained by using proposed PLCS with APCMR controller.

5.4.2 Performance Evaluation Under Grid Impedance Variation (Weak Grid)

In this section, the performance of the proposed PLCS with APCMR and the PLL-less APMR controller (discussed in chapter 4) are investigated under dynamic change in grid impedances. When the grid inductance is L_g= 2 mH, the grid is normal with high SCR (= 4.8). However, when the L_g= 10 mH the grid is weak with low SCR (=1). Fig. 5.14 demonstrates the experimental waveforms during transion from normal grid to weak grid. It is observed from Fig. 5.14 (a)-(b) that both the proposed PLCS with APCMR controller and the PLL-less APMR controller, the grid voltage and grid currents are balanced and sinusoidal under normal grid conditions, when L_g= 2 mH. At time $t = t1$, L_g is increased from 2 mH to 10 mH, and the grid becomes weak due to low SCR. Under the weak grid

conditions, the grid currents are highly distorted (with THD 6.93 %) obtained by PLL-less APMR controller. However, the distortions in the grid currents are very small (around THD 3.15 %) obtained by using the proposed PLCS with APCMR controller. Therefore, it is concluded that under wide grid impedance variations, the oscillations in the grid current are very less using the proposed PLCS with APCMR controller.

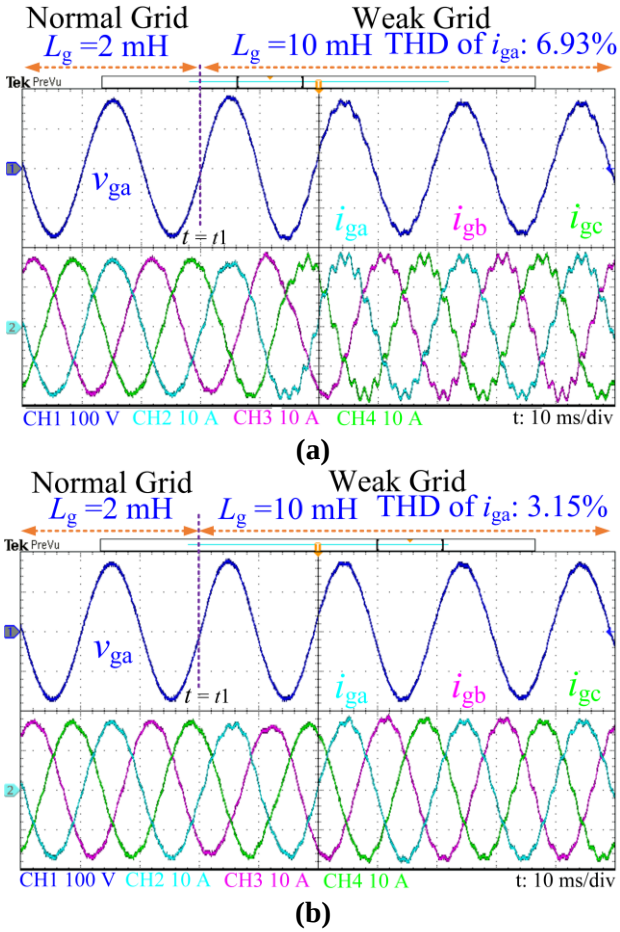

Fig. 5.14. Experimental waveforms of grid voltage (v_{ga}) and grid current (i_{ga}) during sudden change of grid impedance. (a) with PLL-less APMR controller. (b) with proposed PLCS with APCMR controller.

5.4.3 Performance Evaluation with LVRT During Various Grid Faults

In this section, the performance of the proposed PLCS with APCMR controller is investigated with LVRT during asymmetrical grid faults. It is observed from Fig. 5.15(a) that a single line to ground (L-G) fault occurs in phase *a* at t= $t_{f,}$ and the fault is cleared after 100 ms at $t = t_c$. Due to the L-G fault, the magnitude of v_{ga} decreases to 55% of the rated grid voltage. As shown in Fig. 5.15(b), the grid current waveforms are distorted during the LVRT operation, when the conventional PBCS with CPMR controller is applied. When the proposed PLCS with APCMR controller is employed, the grid current is balanced and sinusoidal as the negative sequence currents are suppressed, as shown in Fig. 5.15(c).

It is observed from Fig. 5.15(b) that the THD of the grid current obtained by using the conventional PBCS with CPMR controller is 8.75 %, which is above the stipulated limit of IEEE 519 standards. However, the grid current THD is reduced to 3.9 % using the proposed PLCS with APCMR controller as shown in Fig. 5.15(c). As seen from Fig. 5.15(d), there are twice the grid frequency oscillations in PV voltage, PV power, active and reactive powers injected to grid under LVRT operation with the conventional PBCS with CPMR controller. These oscillations are occurred due to negative sequence components in grid voltages and currents.

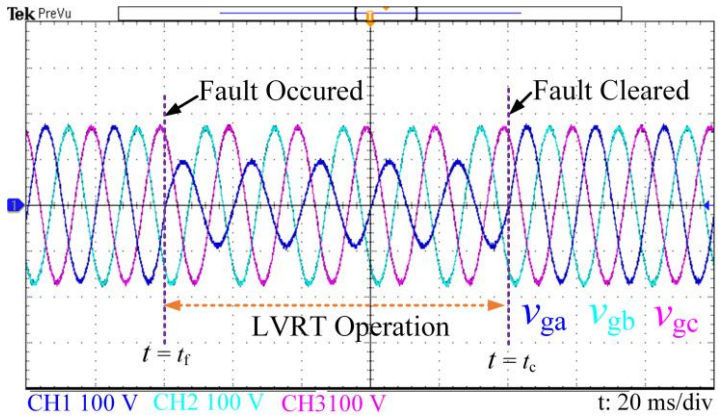

(a)

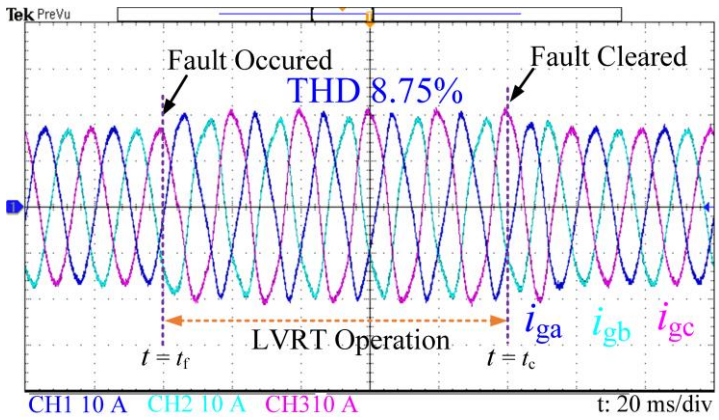

(b)

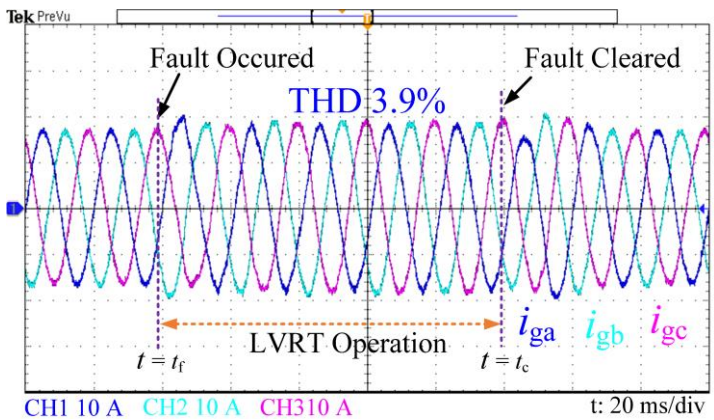

(c)

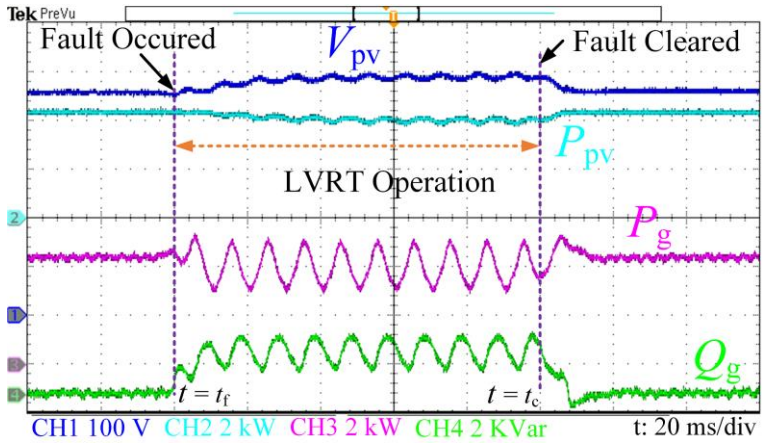

(d)

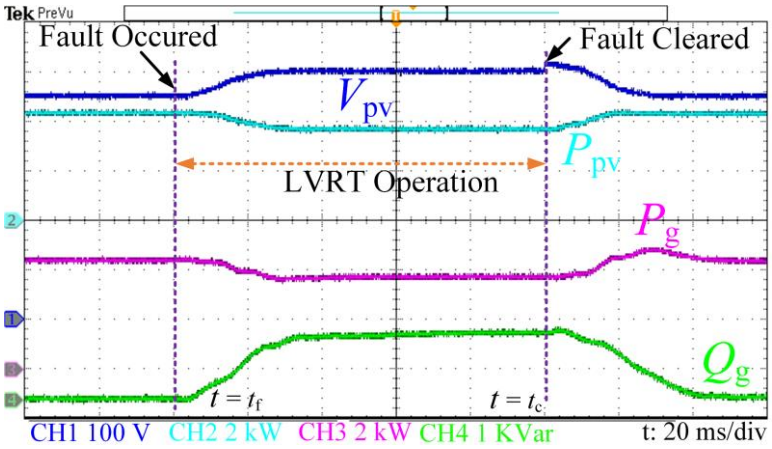

(e)

Fig. 5.15. Experimental waveforms under L-G fault in phase a with grid voltage magnitude 55 % of rated grid voltage. (a) grid voltages (b)-(c) grid currents obtained by using conventional PBCS with CPMR controller and proposed PLCS APCMR controller with PSRCG. (d)-(e) PV voltage, PV power, active and reactive power obtained by using conventional PBCS with CPMR controller and proposed PLCS APCMR controller with PSRCG.

However, as seen from Fig. 5.15(e) the oscillations in PV voltage, PV power, active and reactive powers injected into the grid are eliminated, when the proposed PLCS with APCMR controller is adopted. It is noticed that during LVRT operation, the VSI injects reactive power to the grid, as shown in Fig. 5.15(d)-(e).

Similarly, Fig. 5.16 demonstrates the performance of the grid-tied PV system under an asymmetrical double line to ground faults (L-L-G) with grid voltage magnitudes and phases as $v_{ga} = 120\angle 0°$, $v_{gb} = 66\angle -110°$, $v_{gc} = 78\angle 110°$. The L-L-G grid fault occurs at $t = t_f$, and the fault is cleared at $t = t_c$. As it is observed from Fig. 5.16(b)-(c), the grid current is balanced and sinusoidal with the proposed PLCS with APCMR controller. However, with the conventional PBCS with CPMR controller, the grid currents are not sinusoidal due to the negative sequence component of grid currents. Moreover, as seen from Figs. 5.16 (d)-

(e), when the PV voltage increases, the PV power decreases due to shifting of the operating mode from MPPT mode to LVRT mode. During t= t_f to t= t_c, the VSI starts injecting reactive power for satisfactory LVRT operation. It is noticed that there are significant oscillations in active power, reactive power, PV power and PV voltage by adopting PBCS with CPMR controller. However, these oscillations are eliminated by using the proposed PLCS with APCMR controller.

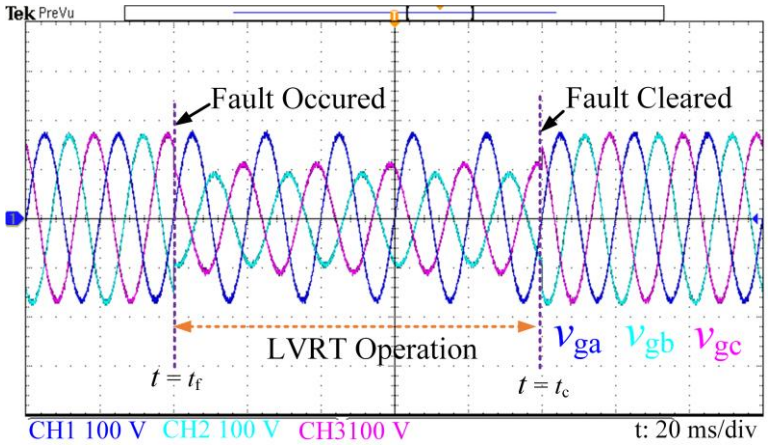

(a)

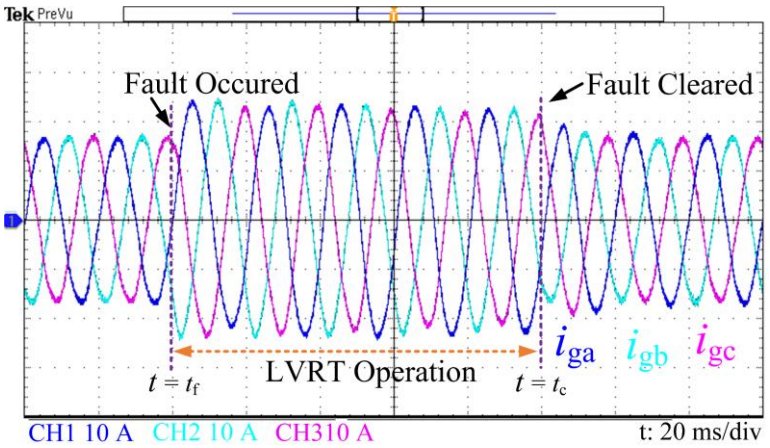

(b)

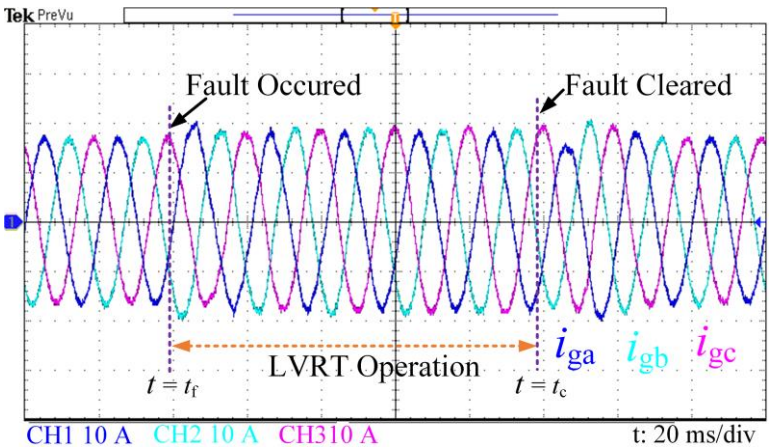

(c)

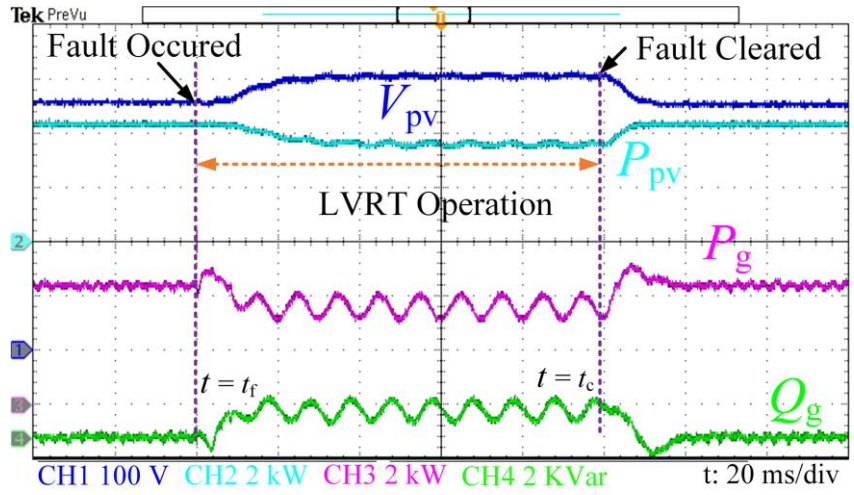

(d)

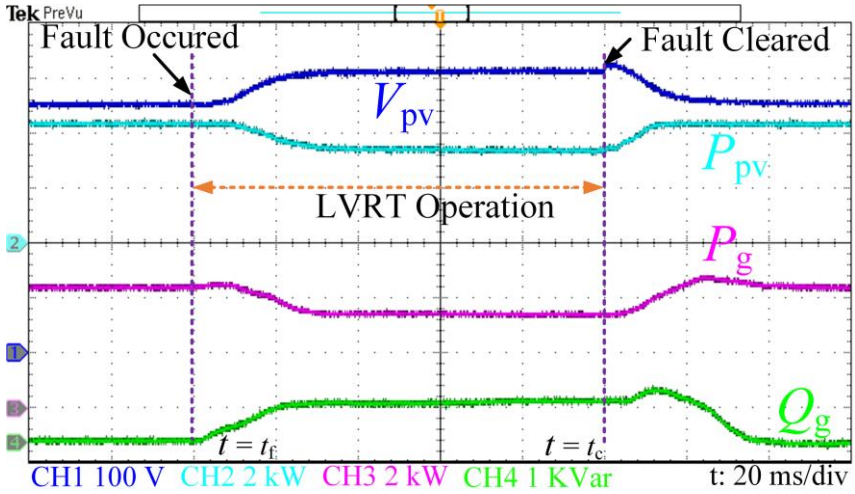

(e)

Fig. 5.16. Experimental waveforms under asymmetrical fault (L-L-G fault) (v_{ga} = 120∠ 0°, v_{gb} =66∠ -110°, v_{gc} =78∠ 110°). **(a)** grid voltages **(b)-(c)** grid currents obtained by using conventional PBCS with CPMR controller and proposed PLCS APCMR controller with PSRCG. **(d)-(e)** PV voltage, PV power, active and reactive power obtained by using conventional PBCS with CPMR controller and proposed PLCS APCMR controller with PSRCG.

5.4.4 Performance Evaluation with Grid Frequency Variations

The dynamic performance of the grid-tied PV system under grid frequency variation from 50 Hz to 52 Hz is shown in Fig. 5.17 to compare the frequency adaptability of the proposed PLCS with APCMR controller with the conventional PBCS with CPMR controller. It is observed from Fig. 5.17(a) that the conventional PBCS with CPMR controller tracks the new grid frequency with frequency tracking time of 80 ms. On the other hand, the proposed PLCS with APCMR controller is not sensitive to grid frequency variations and provides high tracking accuracy with frequency tracking time of 2ms, as evident in Fig. 5.17 (b).

Therefore, it is clear that the proposed PLCS with APCMR controller is robust against grid frequency variations.

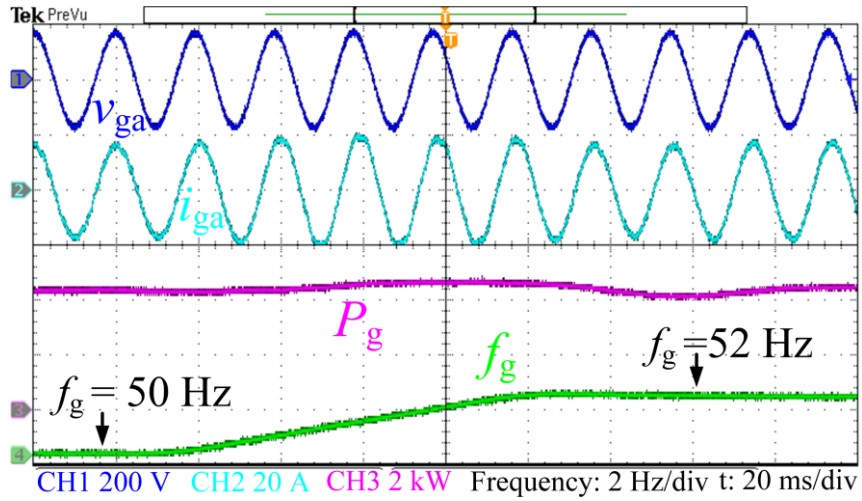

(a)

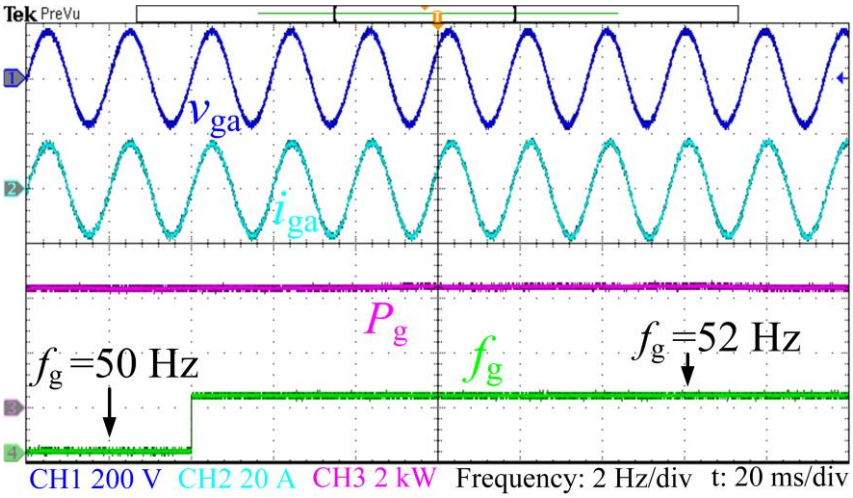

(b)

Fig. 5.17 Dynamic experimental waveforms of the grid voltage (v_{ga}), grid current (i_{ga}), active power (P_g) and grid frequency (f_g) when f_g changes from 50 Hz to 52Hz. (a) with conventional PBCS with CPMR controller. (b) with proposed PLCS with APCMR controller.

5.4.5 Comparative Analysis of the Proposed Control Strategy with the Existing Control Strategies

In this section, a comparison among different existing control strategies is presented in Table 5.3 to bring out the uniqueness and effectiveness of the proposed PLL-less control strategy in terms of various features. It is observed that the proposed control strategy has less computational burden and execution time (3.66%, 0.9 μs) as compared to the active and reactive current control approach (7.12% ,1.9 μs) presented in [129], grid-connected PV power plant (GCPPP) without phase angle synchronization (5.2%, 1.4 μs) discussed in

[127] and multi-objective control approach (7.12%, 1.9 μs) reported in [130]. The proposed control strategy uses basic arithmetic operations such as additions, subtractions, multiplications and divisions, and thus has very low computational burden on OPAL-RT simulator. The proposed control strategy has a faster frequency tracking time (2ms) as compared to active and reactive current control approach (100 ms). The THD of the grid current by using multi objective control strategy and active and reactive current control are 9.06 % and 7.6%, respectively. However, the grid current THD using the proposed control strategy is 2.84 % which is lower than the other control strategies and as per the IEEE 519 standard. It is observed that with the multi objective control strategy, the peak-to-peak active power ripple during grid fault is 1.6 kW which is 37.2 % of the rated grid injected active power. However, with the proposed control strategy, the active power ripple is very low 0.04 kW which is 0.93 % of the rated grid injected active power. Moreover, the grid current magnitude during the fault period is balanced and within the threshold limit using the proposed control strategy. Thus, the performance of the grid-tied PV system during the fault period to meet LVRT is better using the proposed control strategy than the existing control strategies. It is seen from Table 5.3 that the performance of the grid-tied PV system with the proposed control strategy is superior as compared to existing control strategies in terms of reducing the power oscillations, suppression of grid current harmonics, faster frequency tracking capability and reduction in computational burden.

TABLE 5.3. Comparative Analysis of the Proposed control Strategy with Existing Control Strategy.

Features	**Active and reactive current control [129]**	**GCPPP without phase angle synchronization [127]**	**Multi objective control strategy [130]**	**Proposed control strategy**
Need for dedicated PLL	Required	Not required	Required	Not required
Grid current magnitude during fault	High and not balanced	High and not balanced	With in the threshold and balanced	With in the threshold and balanced
Power oscillations	Medium	Medium	High	Very Low
Harmonic current elimination	Poor	Not reported	Poor	Very good
Performance under weak grid	Affected	Affected	Affected	Not affected
Frequency tracking capability	Low	Better	Low	Better
THD of grid current	7.6 %	-	9.06 %	2.84 %

Peak to Peak Active power ripples	1.4 kW	1.4 kW	1.6 kW	0.04 kW
Power ripple (%)	32.5 %	32.5 %	37.2 %	0.93 %
Frequency tracking time during grid frequency deviation	100 ms	2 ms	100 ms	2 ms
Execution time	1.9 μs	1.4 μs	1.9 μs	0.9 μs
Computational burden (%)	7.12 %	5.2 %	7.12 %	3.66 %

5.5 Conclusion

A PLL-less control strategy for a single-stage grid-tied PV system under distorted, weak grid and grid fault conditions is proposed in this chapter. The proposed control strategy successfully achieves enhanced LVRT operation using APR and DRPS controllers during grid faults. The proposed control strategy effectively suppresses the grid current harmonics under weak and distorted grid conditions using the coordinated operation of APR, DRPS and APCMR controllers. Furthermore, PCRCG integrated with the APCMR controller is used to eliminate active and reactive power oscillations and self-synchronize the VSI with the grid. The computational burden on the proposed PLL-less control strategy reduces as the proposed strategy eliminates the PLL block. The comparative analysis of the proposed PLL-less control strategy and the existing control strategies have been discussed. The proposed PLL-less control strategy has been validated experimentally through a 4.3 kW PV power laboratory setup. The experimental results obtained through the proposed PLL-less control strategy demonstrate significant improvement in LVRT capability, grid current harmonics reduction, and power oscillations reduction compared to the conventional PLL-based control strategy. Furthermore, the frequency adaptability of the grid-tied PV system has been improved under grid frequency deviations using the proposed PLL-less control strategy.